Official journal of the JHL 2689-9620
www.light-am.com

Article Open Access

Functional plastic films: nano-engineered composite based flexible microwave antennas with near-unity relative visible transmittance

Cheng Zhang[1,*], Liang Zhu[2], Chengang Ji[3], Zhilu Ye[2], Nabeel Alsaab[2], Minye Yang[2], Yuhui Hu[1], Pai-Yen Chen[2,*] and L. Jay Guo[3,*]

Abstract

Microwave antennas are essential elements for various applications, such as telecommunication, radar, sensing, and wireless power transport. These antennas are conventionally manufactured on rigid substrates using opaque materials, such as metal strips, metallic tapes, or epoxy pastes; thus, prohibiting their use in flexible and wearable devices, and simultaneously limiting their integration into existing optoelectronic systems. Here, we demonstrate that mechanically flexible and optically transparent microwave antennas with high operational efficiencies can be readily fabricated using composite nanolayers deposited on common plastic substrates. The composite nanolayer structure consists of an ultra-thin copper-doped silver film sandwiched between two dielectric films of tantalum pentoxide and aluminum oxide. The material and thickness of each constituent layer are judiciously selected such that the whole structure exhibits an experimentally measured averaged visible transmittance as high as 98.94% compared to a bare plastic substrate, and simultaneously, a sheet resistance as low as 12.5 Ω/sq. Four representative types of microwave antennas are implemented: an omnidirectional dipole antenna, unidirectional Yagi-Uda antenna, low-profile patch antenna, and Fabry-Pérot cavity antenna. These devices exhibit great mechanical flexibility with bending angle over 70°, high gain of up to 13.6 dBi, and large radiation efficiency of up to 84.5%. The proposed nano-engineered composites can be easily prepared over large areas on various types of substrates and simultaneously overcome the limitations of poor mechanical flexibility, low electrical conductivity, and reduced optical transparency usually faced by other constituent materials for flexible transparent microwave antennas. The demonstrated flexible microwave antennas have various applications ranging from fifth-generation and vehicular communication systems to bio-signal monitors and wearable electronics.

Keywords: Optically transparent antenna, Flexible microwave antenna, Transparent conductor, Ultra-thin silver, Doped silver, Wearable optoelectronics

Correspondence: Cheng Zhang (cheng.zhang@hust.edu.cn) or Pai-Yen Chen (pychen@uic.edu) or L. Jay Guo (guo@umich.edu)
[1]School of Optical and Electronic Information & Wuhan National Laboratory for Optoelectronics, Huazhong University of Science and Technology, Wuhan, 430074, China
[2]Department of Electrical and Computer Engineering, University of Illinois at Chicago, Chicago, IL 60607, USA
Full list of author information is available at the end of the article.

Introduction

Rapid ongoing development of smart city, vehicular communication, fifth-generation (5G) network, and internet-of-things (IoTs) requires new hardware technology that allows more efficient use of space, power, and

communication bandwidth.[1,2] One effective and economical solution is to embed additional data access points and signal interrogators into existing infrastructures by deploying optically transparent microwave antennas onto vehicles, building windows, solar panels, communication facilities, etc[3–5]. Similar to traditional microwave antennas which are typically opaque, optically transparent antennas (OTAs) possess the same functionalities and can efficiently collect, process, as well as transmit microwave signals. In addition, they are transparent in the visible and near-infrared (IR) regions, rendering them easy to integrate with diverse optoelectronic devices, such as solar cells, displays, photodetectors, and more. For various practical applications, the OTAs are highly desirable to be fabricated on flexible substrates and applied over curved surfaces, such as skin, clothes, optical fibres, and vehicle windows[6].

Early exploration of OTAs utilises transparent conductive oxides, such as Indium Tin Oxide (ITO) and Fluorine doped Tin Oxide (FTO), which exhibit high optical transparency (e.g. an averaged transmittance of ~ 85% or higher in the visible range) and low electrical resistivity (e.g. a sheet resistance of ~ 30 Ω/sq)[7–9]. However, transparent conductive oxides are brittle; thus, susceptible to cracking when bent, which makes them unsuitable for flexible device applications[10]. Consequently, there have been intensive research efforts to develop flexible OTAs based on ITO-free materials over recent years. Currently, several alternative materials have been exploited, including conductive polymers[11], carbon-based materials[12,13], and metal meshes[14]. Conductive-polymer-based OTAs can be conveniently fabricated on flexible substrates by screen-printing or inkjet-printing[15]. However, they generally exhibit reduced efficiency compared to traditional devices using opaque metals owing to the low conductivity of the polymer. In addition, conductive-polymer-based OTAs typically display certain colours and lack sufficient environmental stability, further limiting their practical usage. Carbon-based materials, such as graphene, can provide good mechanical flexibility and decent optical transparency[16,17]. However, their relatively large sheet resistance may be a limiting factor for microwave antenna applications. Although metal meshes can provide low electrical resistivity by delicately controlling the ratio of opening areas over their surfaces, they generally suffer from sacrificed optical transmittance. In addition, they require relatively complex patterning processes, and their crisscross topology with patterned opaque materials might affect the antennas' aesthetic appearance[18–20]. In contrast to the above candidates, thin metal films show great potential for flexible OTA applications owing to their low electrical resistance and decent optical transmittance. Moreover, large-area and defect-free metal films can be readily prepared on flexible substrates using various physical vapour deposition (PVD) methods, such as evaporation and sputtering[21,22]. However, thin-metal-film-based OTAs inevitably encounter a trade-off between antenna transparency in the visible (high-frequency) region and radiation performance in the microwave (low-frequency) region. Specifically, decreasing the thickness of the metal film can increase the visible transparency of the device. However, this reduces the electrical conductivity of the film and deteriorates the performance of the OTA in the microwave region.

Here, we demonstrate a novel thin-metal-film-based flexible OTA platform using a nano-engineered dielectric-metal-dielectric (DMD) composite structure, which effectively overcomes the aforementioned trade-off between the optical transmittance and radiation performance of the antenna. An ultra-thin (7 nm), smooth, and highly conductive (sheet resistance ~ 12.5 Ω/sq) copper-doped silver film is employed as the central metal layer, which simultaneously guarantees the antenna's high optical transmittance and low electrical resistance. Moreover, two dielectric layers of judiciously selected constituent material and film thickness are utilised to sandwich the thin doped Ag layer, which further promotes the antenna's neutral colour appearance and enhances its optical transmittance, leading to an unprecedently high averaged relative visible transmittance of 98.29%. Using the developed device architecture, we experimentally demonstrate several individual and arrayed OTAs of decent performance, including (*i*) flexible planar dipole antenna that operates at 2.5 GHz and exhibits omnidirectional radiation pattern with a realised gain of −0.67 dBi; (*ii*) unidirectional planar Yagi-Uda antenna with a realised gain of 4.6 dBi at 2.8 GHz; (*iii*) patch antenna working in the C-band (4−8 GHz) with broadside radiation properties and gain up to −1.3 dBi at 5.8 GHz; (*iv*) high-gain Fabry-Pérot (FP) cavity antenna with a realised gain of 13.6 dBi at 8.1 GHz. The demonstration of these antenna representatives serves to illustrate the capabilities of the optically transparent DMD composite structure in supporting a diverse range of antenna designs and radio-frequency (RF) applications. This study provides an insight for the development of compact, efficient, and flexible OTAs that can be employed in an array of applications, including 5G and vehicular communication systems, wearable electronics, self-powered devices, and the IoTs.

Results and Discussion

Candidate materials for thin-metal-film-based OTAs include Ag, Cu, and Au[23]. Among them, Ag stands out by

its highest electrical conductivity at microwave frequencies and lowest optical loss in the visible regime[24]. However, Ag films deposited using common sputtering or evaporation techniques are characterized by less-than-ideal structural stability, as well as large surface roughness resulting from the intrinsic 3D (Volmer-Weber) growth mode of Ag atoms, which precludes the formation of continuous and defect-free Ag films of thickness below ~ 15 nm[23]. Increasing film thickness to the range of 15−25 nm mitigates the issue of dis-continuous film formation and rough surface morphology; thus, achieving good electrical conductivity for microwave antenna applications. However, the visible transparency of the antenna is inevitably sacrificed owing to the large reflection and absorption losses caused by the thick metal film.

We recently demonstrated a new approach to fabricate ultra-thin (down to 6 nm) and ultra-smooth (RMS surface roughness < 1 nm) Ag films by doping a small amount of the second metal (e.g., Al, Cu, Ni, Ti, or Cr) during Ag deposition[25,26]. In addition, we have employed doped Ag in several optoelectronic devices, including organic solar cells[27], polymer light emitting diodes[28], plasmonic waveguides[29], hyperbolic metamaterials[30], and electromagnetic shielding coatings[31,32]. By adding a proper amount of second metal during the Ag deposition, the intrinsic 3D growth mode of Ag atoms is largely suppressed; consequently, ultra-thin and high-quality Ag films can be obtained on various substrates. A detailed analysis is provided in Ref. 26 and 29. Here, by leveraging this novel material, we exploit its application in high-performance flexible OTAs based on a dielectric-metal-dielectric (DMD) composite structure on a polyethylene terephthalate (PET) plastic substrate (Fig. 1a, b). The central metal film in the DMD structure acts as a conductive medium, whose resistivity largely determines the performance of the OTA in the microwave region. For this purpose, we employ Cu-doped Ag as it exhibits the lowest optical loss and best electrical conductivity among different doped Ag films, as indicated in our previous study[28]. To implement flexible OTAs, we utilise a 7-nm-thick Cu-doped Ag film with a measured sheet resistance as low as 12.5 Ω/sq, sufficient for most high-efficiency microwave antenna applications. The deposited film exhibits a smooth and defect-free surface morphology (Fig. 1c), with an AFM-measured surface roughness value as low as 0.42 nm[28]. This significantly minimises electron scattering loss at the film surface and grain boundaries, leading to a high optical transmittance and low sheet resistance.

To further enhance the visible transmittance and colour neutrality of the antenna, we sandwich the thin Cu-doped Ag layer between two dielectric films. The employed dielectric layers help match the impedance of the surrounding media; thus, significantly suppressing reflection from the DMD structure. In addition, they act as protective layers that prevent environmental damage to the thin Ag film and guarantee the operational stability of the antenna. To maximise the antireflection effect, a dielectric material with a high refractive index in the visible (Ta_2O_5[33] in this case) is employed for the layer on the substrate side, and a material with a lower refractive index (Al_2O_3 in this case) is used for the layer on the air side. The associated layer thicknesses are judiciously chosen to achieve maximum visible transmittance and neutral colour appearance simultaneously. When the film thicknesses of the Ta_2O_5 and Al_2O_3 layers are 36 nm and 65 nm, respectively, corresponding to a total structural thickness of 108 nm, the calculated visible transmittance through the DMD structure reaches a peak value (Fig. 1d). For the wavelength of interest in this study (400−800 nm), the structure exhibits a high and flat transmission spectrum (Fig. 1e, dash line). When compared with a bare PET substrate, the average transmittance is as high as 99.57%, reaching a near-unity visible transparency. Transmission through a 7-nm-thick Cu-doped Ag film on a PET substrate is plotted in Figure S1, Section I of the Supporting Information. To further evaluate the colour appearance of the structure, the calculated transmission spectrum is converted into coordinates in the $L^*a^*b^*$ colour space, as defined by the International Commission on Illumination. The L^* value is calculated to be 98.99, indicating high optical transparency. The a^* and b^* values are calculated to be −0.70 and 0.41, respectively, indicating a neutral colour appearance.

The enhanced optical transparency of the nanocomposite can be attributed to the broadband transmission resonances induced by the two dielectric layers. To reveal this effect, the net phase accumulation inside each dielectric layer, φ, is calculated. The phase accumulation includes both the reflection phase shifts at the two interfaces and the propagation phase through the dielectric layer. A transmission resonance, which contributes to the enhanced optical transmittance, occurs when the aforementioned net phase accumulation equals multiples of 2π radians. As shown in Fig. 1f, a single transmission resonance inside the Al_2O_3 layer is located at free-space wavelength λ_0 = 474 nm, and several transmission resonances inside the Ta_2O_5 layer are located at λ_0 = 449, 572, and 707 nm, respectively. Owing to the low reflectance at both the top and bottom interfaces of each dielectric layer, the transmission resonances are weakly confined inside the

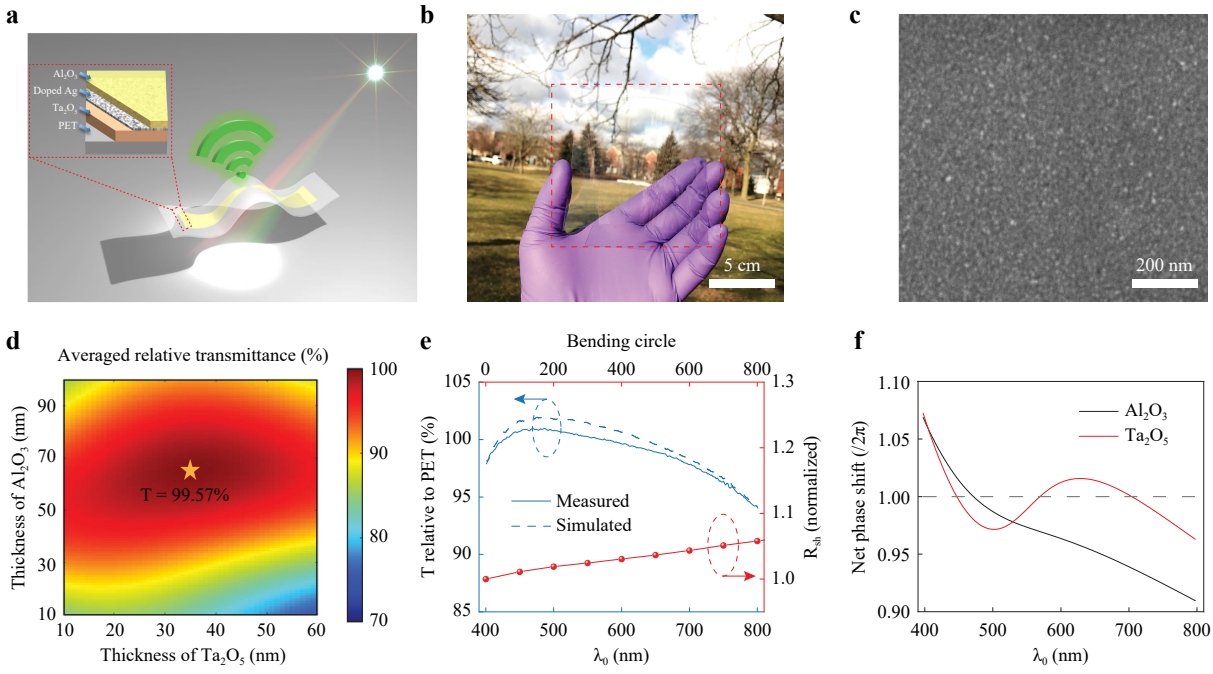

Fig. 1 **a** Schematic illustration of the proposed optically transparent antenna consisting of layers of Ta_2O_5, Cu-doped Ag, and Al_2O_3 on a flexible PET substrate. **b** Photo of a nanocomposite structure deposited on a PET substrate showing a close-to-unity relative visible transmittance. **c** Scanning electron microscope (SEM) image of a 7-nm-thick Cu-doped Ag film exhibiting a smooth surface morphology. **d** Calculated averaged visible (400−800 nm) transmittance of the Ta_2O_5 / Cu-doped Ag / Al_2O_3 nanocomposite structure, where transmittance through a bare PET substrate is used for reference. When the thicknesses of the Ta_2O_5 and Al_2O_3 layers are respectively set to 36 nm and 65 nm, the averaged relative transmittance reaches a peak value of 99.57%. **e** Left: Simulated (dashed blue curve) and measured (solid blue curve) relative transmission spectra of the nanocomposite structure. Right: Change in sheet resistance of the structure as a function of bending cycles (bending radius: 0.25 inch). The structure shows a ~6% increase in sheet resistance after 800 cycles of bending. **f** Calculated net phase shifts inside the Al_2O_3 layer (black curve) and Ta_2O_5 layer (red curve) as a function of free-space wavelength for the proposed nanocomposite structure made of 36-nm-thick Ta_2O_5 / 7-nm-thick Cu-doped Ag / 65-nm-thick Al_2O_3. A transmission resonance, which contributes to the structure's enhanced visible transparency, occurs when the net phase shift equals multiples of 2π radians.

cavity; thus, exhibit broad spectral bandwidths. Consequently, they overlap in the spectral domain, leading to a high and flat transmission spectrum of the nanocomposite.

The nano-engineered composite-based flexible microwave antennas are fabricated by sequentially sputtering Ta_2O_5, Cu-doped Ag, and Al_2O_3 layers onto plastic substrates. The thicknesses and refractive indices of the deposited films are characterised using spectroscopic ellipsometry (see Experimental Section for details). The measured transmission spectrum of the sample is plotted in Fig. 1e (solid line), which corresponds well to the simulated curve and exhibits an averaged relative transmittance of 98.94 ± 0.24%. The associated *L*a*b** values are calculated to be 98.61 ± 0.09, −0.50 ± 0.01, and 0.22 ± 0.03, respectively, which also agree well with numerically predicted values. The cited uncertainties represent one standard deviation from the measured data. In addition, the structure demonstrates exceptional mechanical flexibility, as shown in Fig. 1e, where the sheet resistance (R_{sh}) remains nearly unchanged after 800 bending cycles (bending radius: 0.25 inch). These characterization results confirm the superiority of our nanocomposite over existing transparent conductor materials for both flexible and rigid OTA applications in terms of electrical conductivity and optical transparency. A comparison of the critical parameters of different candidate materials is listed in Table 1. Notably, most of these candidate materials exhibit optical transmittance levels below or around 80%, limiting their suitability for applications requiring high optical transparency. Conversely, materials with higher transmittance typically compromise the electrical conductivity, potentially affecting the antenna gain and efficiency. Thus, simultaneously achieving high transparency and conductivity is challenging. However, our proposed nanocomposite structure exhibits exceptional performance, achieving a record-high transmittance level of up to 98.3%

Table 1 Comparison of the key parameters of different candidate materials for OTA applications

Ref.	Material	Sheet Resistance (Ω/sq)	Measured Optical Transmittance	Wavelength Range
34	Conductive polymer	0.08	62.5% (a. T.)	@ 550 nm
20	ITO	15	72% (a. T.)	380 – 750 nm
20	Metal mesh	0.048	69.8% (a. T.)	380 – 750 nm
19	Metal mesh	0.5	70% (a. T.)	400 – 700 nm
35	Metal mesh	0.18	62.1% (a. T.)	400 – 800 nm
35	Multilayer film	2.52	68.63% (a. T.)	400 – 800 nm
36	Graphene	18	85% (a. T.)	350 – 900 nm
37	Three-layer stacked graphene	80	90.4% (a. T.)	@ 550 nm
38	FTO/ITO	4	75% (a. T.)	400 – 800 nm
39	AgNW	8.5	85% (a. T.)	@ 550 nm
40	Ag/Ti	0.017	59.2% (a. T.)	400 – 800 nm
40	ITO/Ag/ITO	5.05	71.3% (a. T.)	400 – 800 nm
			89.7% (a. T.)	400 – 800 nm
This work	Ta_2O_5/Cu-doped Ag/Al_2O_3	12.5	91.4% (a. T.)	@ 550 nm
			98.3% (r. T.)	400 – 800 nm

(Notes: 'a.T' means absolute transmittance, and 'r.T' means relative transmittance over that of the substrate)

across a broad wavelength spectrum, while maintaining a comparatively low sheet resistance. This combination of properties renders it an ideal candidate for OTA applications.

We utilise the obtained highly transparent and flexible nanocomposites to implement several OTAs of representative microwave-shaping functionalities, which respectively operate within the fourth-generation long-term-evolution (4G-LTE) band (e.g. 1.7 GHz and 1.9 GHz band), Bluetooth band (2.4 GHz), and Wi-Fi channels (2.4 GHz and 5.9 GHz bands). The first OTA is a half-wave dipole antenna commonly used as a TV or broadcasting antenna in wireless communication networks[41,42]. A schematic illustration of the implemented flexible dipole antenna is shown in Fig. 2a, where the alternating currents on its two dipole arms oscillate in phase to generate omnidirectional RF radiation. The resonant frequency of the dipole antenna can be tuned by adjusting its arm length. Three devices ($D_{2.0}$, $D_{2.5}$, and $D_{4.2}$) with resonant frequencies of 2.0 GHz, 2.5 GHz, and 4.2 GHz are implemented. The antennas have the same arm width (w = 13 mm) and separation gap (g = 3 mm), and their arm lengths (L) are respectively chosen as 25.0 mm ($D_{2.0}$), 17.5 mm ($D_{2.5}$), and 8.0 mm ($D_{4.2}$). The measured reflection spectra (return loss, S_{11}) are shown in Fig. 2b, where the resonant frequencies correspond well with simulated ones (Fig. 2b)[43]. The three antennas exhibit operating bandwidths of 0.82 ± 0.02 GHz ($D_{2.0}$), 0.77 ± 0.04 GHz ($D_{2.5}$), and 0.91 ± 0.04 GHz ($D_{4.2}$), respectively, with return losses exceeding 10 dB. Typically, the measured antenna properties may exhibit slight disparities compared to the simulated properties. This primarily stems from the idealised conditions underpinning the simulation, falling short of fully considering complex real-world scenarios, such as multipath propagation, cable and connecter losses, and fabrication imperfections. In our case, the disparities between the simulation and measurement results, although present, remain relatively modest and well within the acceptable margins. The simulation continues to demonstrate commendable accuracy in predicting the experimental measurements. In addition, the experimentally measured resonant frequencies match well with the numerical calculations based on empirical equations (Fig. 2c). The details of the calculation process are presented in Section II of the Supporting Information. The red solid lines in Fig. 2d plot the characterised radiation patterns of the $D_{2.5}$ OTA on the *E*- and *H*-planes, showing a maximal realised gain of −0.67 ± 0.22 dBi. Its radiation performance is similar to that of dipole antennas made of opaque materials, such as Ag ink (denoted by blue lines in Fig. 2d) and Cu paste (denoted by black lines in Fig. 2d), and comparable to the reported state-of-the-art transparent dipole antennas[16,17,20]. Moreover, our OTAs provide a close-to-unity relative visible transmittance, which is considerably greater than previously reported results. Similar findings are observed

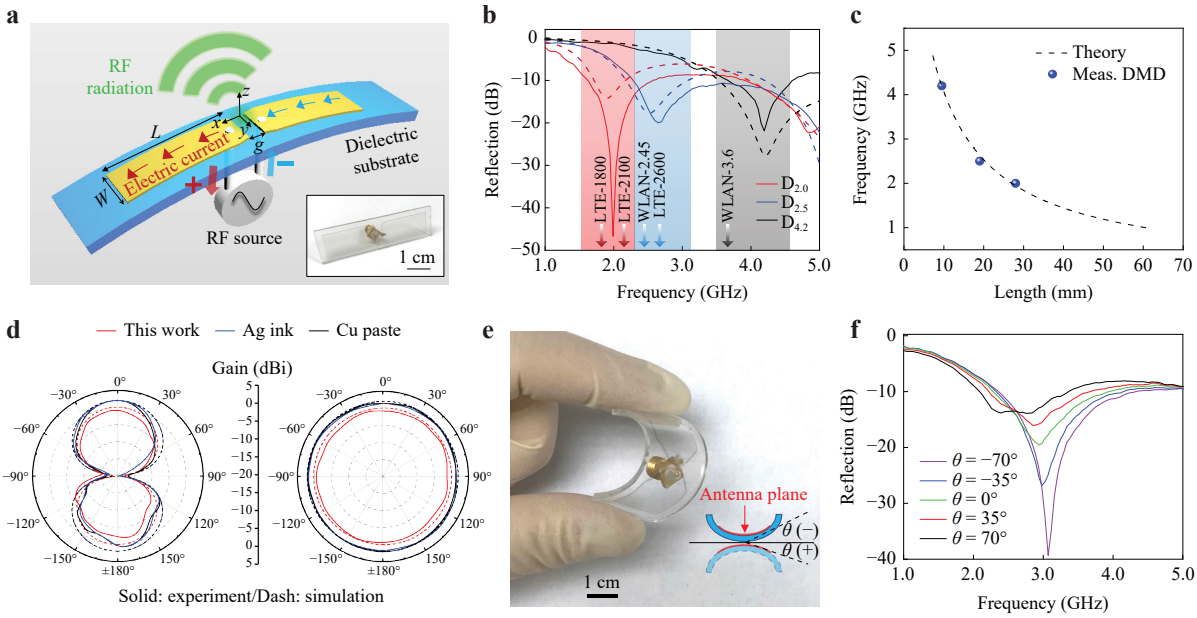

Fig. 2 a Schematic illustration of a flexible transparent dipole antenna made of the proposed nanocomposite. The inset shows a photo of a 2.0 GHz dipole antenna mounted on rigid acrylic substrate. The red and blue arrows represent the two polarities of the electric current. **b** Measured (solid curve) and simulated (dashed curve) reflection spectra of three transparent dipole antennas designed for operation in the 4G/5G wireless communication band, which include several commonly used bands such as LTE-1800, LTE-2100, and WLAN-2.45. **c** Measured resonant frequencies of the nanocomposite-based dipole antennas with different arm lengths, which show close correspondence to the theoretical curve. **d** Measured realised gain as a function of observation angle (radiation pattern) on the *E* (*x*-*z*) plane (left panel) and *H* (*y*-*z*) plane (right panel) for three 2.5 GHz dipole antennas, whose arms are respectively made of the proposed nanocomposite (red lines), silver ink (blue lines), and copper paste (black lines). **e** Photograph of a hand-bent transparent dipole antenna mounted on a polydimethylsiloxane (PDMS) substrate, showing its excellent flexibility. **f** Measured reflection spectra of the antenna at different bending angles.

for the nanocomposite-based OTAs operating at 2.0 GHz and 4.2 GHz (Section III, Supporting Information). Owing to the extremely thin nanocomposite structure, we characterise OTA mounted on a flexible polydimethylsiloxane (PDMS) substrate. The experimental findings demonstrate the remarkable flexibility and foldability of the OTA (Fig. 2e, f). Notably, the resonant frequency and −10 dB bandwidth exhibit only minor fluctuations across a range of bending angles ($-70° < \theta < 70°$). Note that these slight variations have negligible impact on the antenna's performance for practical applications, as the antenna consistently maintains S_{11} below −10 dB in close proximity to its operating frequency (~3 GHz). The flexible OTA also demonstrates robust performance after cyclic bending (Section IV, Supporting Information). However, such results may not be easily achieved with other transparent (e.g. ITO) or opaque (e.g. silver ink and copper) antennas owing to their relatively rigid surfaces and thick conductive coatings.

We demonstrate a high-gain Yagi-Uda OTA with unidirectional radiation properties for shortwave communication and broadcasting applications[44,45]. The Yagi-Uda OTA is designed to resonate at a centre frequency of 2.5 GHz, and all its driven and parasitic elements (reflectors and directors) are made of the nano-engineered composite (Fig. 3a, b). The details of the geometric parameters of the antenna are elaborated in Section V of the Supporting Information. Microwave emission is first sourced from the driving element (i.e. a half-wave dipole operating at 2.5 GHz), and the reflector and other parasitic elements re-radiate waves to form constructive (destructive) interference in the forward (backward) direction, creating a unidirectional radiation pattern. Fig. 3c displays the reflection spectrum of a fabricated Yagi-Uda OTA, where the simulated and measured results correspond well with each other[43], showing a 0.87 ± 0.05 GHz bandwidth centered at 2.5 GHz. The calculated and measured radiation patterns (Fig. 3d, e) are in good agreement with each other, showing unidirectional radiation with a front-to-back ratio of 6.2 ± 0.33 dB and a maximum measured gain of 2.9 ± 0.32 dBi at 2.5 GHz. The cited uncertainties represent one standard deviation from the measured data. Compared to the omnidirectional dipole in Fig. 2, the Yagi-Uda OTA

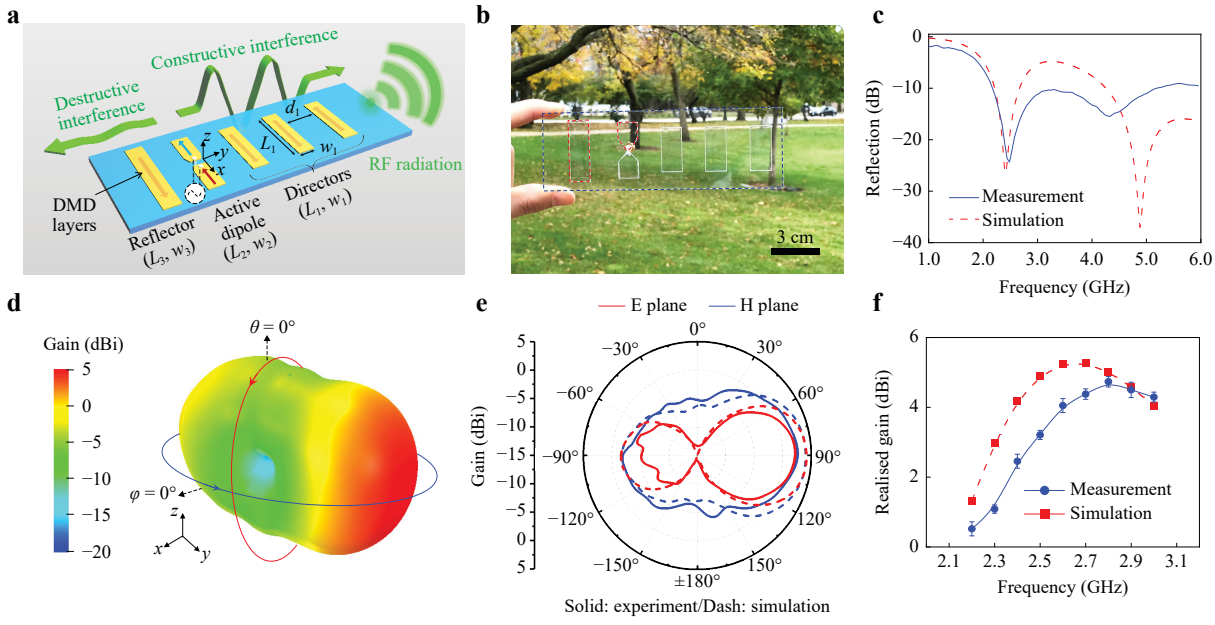

Fig. 3 a Schematic illustration of the high-gain Yagi-Uda OTA with unidirectional radiation property. **b** Photo of a fabricated sample. **c** Measured and simulated reflection spectra of the Yagi-Uda OTA. **d** Calculated three-dimensional (3D) radiation pattern of the Yagi-Uda OTA operating at 2.5 GHz. **e** Measured two-dimensional (2D) radiation patterns of the Yagi-Uda OTA operating at 2.5 GHz. The measured and simulated results are represented by solid and dashed lines, respectively. **f** Measured and simulated realised gain as a function of operating frequency for the Yagi-Uda OTA.

exhibits a higher directivity and larger gain within its operational band (Fig. 3f) owing to constructive interference in the forward propagating direction. The realised gain can be further improved by increasing the number of transparent directors or using a double-layer antenna configuration[46,47].

Next, we demonstrate a group of low-profile, transparent microstrip patch antennas that operate in the C-band (4−8 GHz) and X-band (8−12 GHz), covering the WLAN-5.8 and satellite communication frequencies[48,49]. A microstrip patch antenna is similar to an open cavity with magnetic walls, where the fringing electric fields at the edges are equivalent to magnetic currents that oscillate in phase to generate broadside radiation (Fig. 4a). Fig. 4b shows a photograph (top view) of the fabricated transparent patch antenna, which resonates at 5.8 GHz and is fed by a coaxial cable. Fig. 4c plots the reflection spectra of three patch antennas ($P_{5.8}$, $P_{6.5}$, and $P_{8.2}$) with different patch dimensions, which respectively resonate at 5.8 GHz, 6.5 GHz, and 8.2 GHz (throughout the C-band and X-band). Details of the antenna dimensions are provided in Section VI of the Supporting Information. The measured resonant frequencies correspond well with the analytically calculated frequencies (Fig. 4d; details of the analytical calculation are discussed in Section VII, Supporting Information). Fig. 4e displays the measured *E*-plane (left) and *H*-plane (right) radiation pattern of the patch antenna $P_{5.8}$ with a realised gain of −1.3 ± 0.16 dBi, indicating that the device functions well in the C- and X-band. As shown in Fig. 4e, the realised gain and radiation efficiency of the OTAs may be lower than those constructed from commonly used metals (e.g. Ag and Cu) and substrate materials (e.g. FR-4 and Rogers). This deficiency arises from additional losses in both the conductive and substrate materials. However, it is imperative to emphasise that despite the marginally reduced efficiency, our OTAs offer unparalleled transparency and high flexibility, which are unattainable for traditional antennas relying on printed circuit board technology.

Finally, we implement a highly directional Fabry-Pérot (FP) cavity antenna[50,51], designed to resonate at 8.2 GHz (Fig. 5a). The antenna's key part is a "visible-region-transparent" and "microwave-region-reflective" metasurface made of the proposed nanocomposite. The metasurface, acting as a partially reflective surface (PRS) for the FP cavity antenna, is formed using subwavelength nanocomposite square patches arrayed over the PET surface. Based on the ray-tracing method, multiple reflections occurring between the partially reflective metasurface and the ground plane of the antenna can form a highly directive beam at the broadside. Fig. 5b shows a photograph of the fabricated antenna, where its constituent

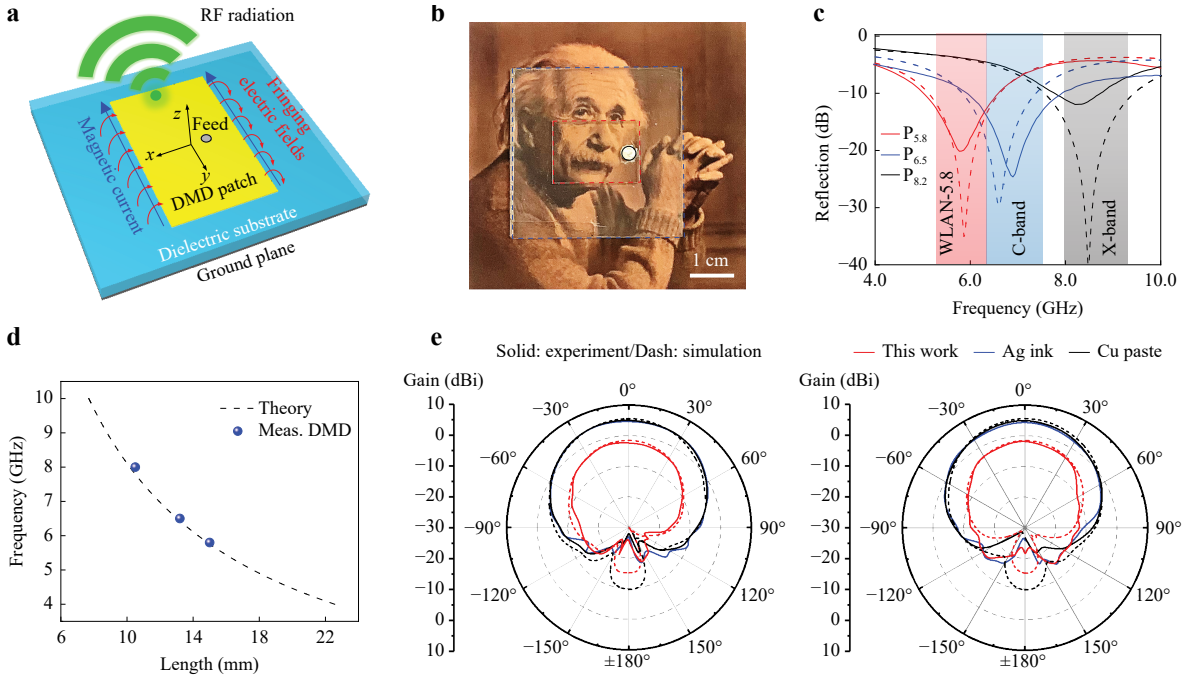

Fig. 4 a Schematic illustration of the low-profile, transparent microstrip patch antenna. **b** Photo of a fabricated sample. **c** Measured (solid line) and simulated (dashed line) reflection spectra of three different transparent patch antennas, $P_{5.8}$, $P_{6.5}$, and $P_{8.2}$, with operating frequencies respectively centered at 5.8 GHz, 6.5 GHz, and 8.2 GHz. **d** Measured resonant frequencies of patch antennas with different patch lengths, which show close correspondence to the theoretical curve. **e** Measured *E*-plane (left panel) and *H*-plane (right panel) radiation patterns of the 5.8 GHz patch antennas, which are respectively made of the proposed nanocomposite (red lines), silver ink (blue lines), and copper paste (black lines).

PRS metasurface is separated from the copper ground plane by a suitable distance h = 19 mm. The ground plane is covered with a paper painting of "The Great Wave off Kanagawa". The FP cavity of the antenna is excited using a small patch antenna located underneath the ground plane. The transparent metasurface acts as a protective layer for the painting and simultaneously reshapes and focuses the radiation from the patch antenna source. Fig. 5c shows the simulated and measured reflection spectra of the FP cavity antenna (with the metasurface) and the source patch antenna (without the metasurface). It can be observed that the FP cavity antenna exhibits a resonant frequency of 8.1 GHz, similar to that of its source patch antenna. The simulated and measured radiation performances of this FP cavity antenna, which correspond well, are shown in Fig. 5d, e, respectively. The device exhibits a realised gain of up to 13.6 ± 0.33 dBi, and good co- and cross-polarisation isolation levels up to 22 ± 0.64 dB at the centre frequency. Compared to its source patch antenna (with a realised gain of 6.5 ± 0.24 dBi), the realised gain of the FP antenna with the transparent metasurface is remarkably enhanced (Fig. 5f). This high realised gain can benefit various long-distance shortwave communication and sensing applications.

Recently, there has been a growing interest in building multifunctional IoT nodes, which seamlessly integrate optical devices and microwave antennas for high-efficiency information transmitting and broadcasting in wireless sensor networks. In this regard, the Fabry-Pérot cavity antenna with a transparent metasurface PRS allows easy vertical integration of various optical devices with microwave-radiating apertures; thus, facilitating a practical and cost-effective realisation of compact monolithically integrated IoT nodes. Additionally, the transparent metasurface, with strategic design and integrated control devices (e.g. diodes), may be extended to programmable metasurfaces that hold the potential for dynamic electromagnetic wave manipulation[52,53]. In particular, the suggested OTAs, distinguished by their exceptional optical transmittance and radiation efficiency, offer promise for a diverse range of applications beyond the capabilities of conventional opaque antennas and existing OTAs. For example, these OTAs can be integrated into automobile windshields to facilitate satellite communication and into eyeglasses for IoT applications. Furthermore, their ultra-thin and flexible nature allows integration onto curved surfaces, such as human skin and clothes, underscoring their potential for wearable applications.

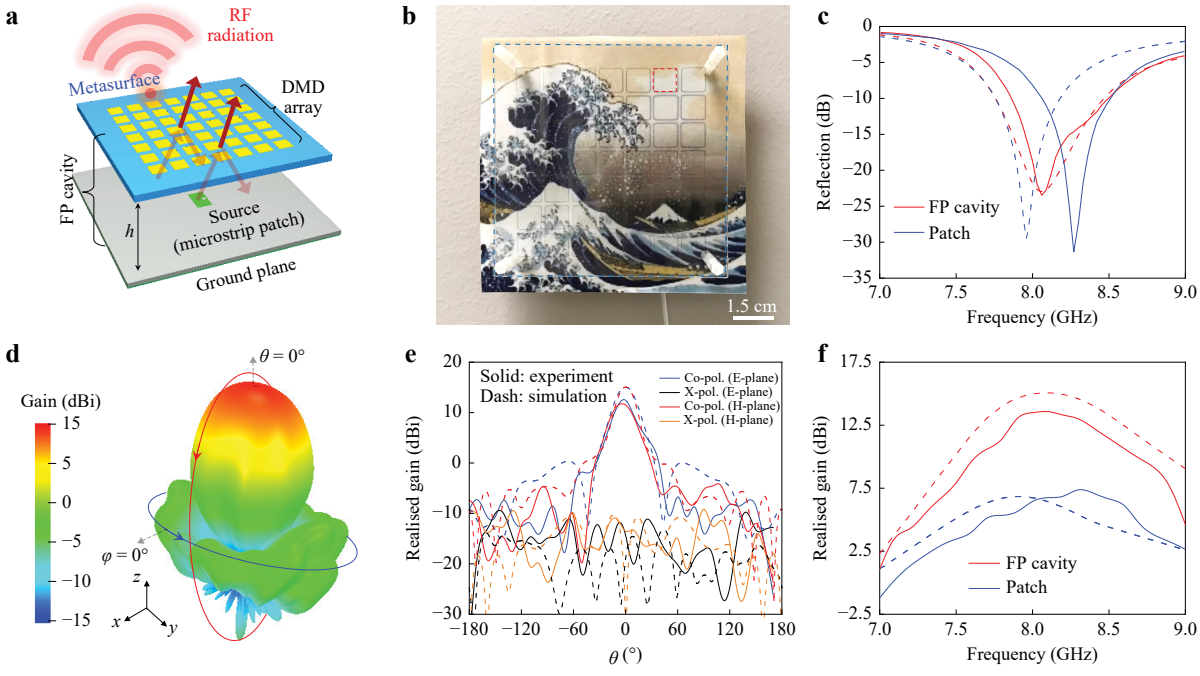

Fig. 5 a Schematic illustration of the Fabry-Pérot cavity antenna, consisting of a transparent metasurface separated from the ground plane by a distance of *h*. A small microstrip patch antenna located underneath the ground plane acts as the feeding source of the cavity antenna. **b** Photo of a fabricated sample. The antenna's ground plane is covered with a paper painting of "The Great Wave off Kanagawa". **c** Reflection spectra for the Fabry-Pérot cavity antenna and the patch-antenna source. The solid and dashed lines represent the measured and simulated results, respectively. **d**–**e** Calculated and measured radiation patterns for the antenna operating at 8.2 GHz. Here, the *E* and *H* planes correspond to the *x*-*z* and *y*-*z* planes, respectively. The measured cross-polarization patterns are also displayed here to show the good co- and cross-polarization isolation level of this antenna. **f** Realised gain against frequency response for the Fabry-Pérot cavity antenna and its patch source, where the Fabry-Pérot cavity antenna shows an obviously enhanced gain.

Conclusions

In this study, we develop a highly transparent and conductive nanocomposite structure comprising Ta_2O_5 / Cu-doped Ag / Al_2O_3 thin layers that can be easily fabricated on flexible substrates using simple and low-cost physical vapour deposition methods. This nanocomposite structure, when used to build microwave OTAs, outperforms traditional constituent materials, including metal meshes and organic polymers, owing to its broadband optical transmittance, low sheet resistance, and excellent mechanical flexibility. The fabricated structure exhibits an averaged visible transmittance as high as 98.29% compared to a bare plastic substrate, and simultaneously, a sheet resistance as low as 12.5 Ω/sq. We demonstrate different types of omnidirectional (dipole) and unidirectional (Yagi-Uda and patch) antennas with operating frequencies covering the S, C, and X bands (1.5−12 GHz), which accommodate most WiFi, Bluetooth, WLAN 5.8, 4G/4G-LTE, and short-range 5G communication applications. Moreover, we implement an optically transparent metasurface, which is employed as the radiating facet of a microwave Fabry-Pérot antenna to achieve a realised gain of up to 13.6 dBi. The demonstrated transparent and flexible nanocomposite structure offers a viable solution for building compact and multifunctional intelligent systems that breaks the lateral design limitation faced by opaque devices and allows vertical integration of "invisible" RF and microwave components with diverse optical devices. Our findings have widespread applications in wearable wireless electronics, IoTs, smart cities, vehicular communications, and next-generation wireless communication infrastructures.

Experimental Section

Device fabrication: Layers of Ta_2O_5, Cu-doped Ag, and Al_2O_3 were sequentially sputter-deposited onto flexible PET substrates. The Ta_2O_5 film was deposited using a Ta_2O_5 target through a reactive radio-frequency (RF) sputtering process with an oxygen flow rate of 2 standard cubic centimetres per minute (sccm). The calibrated deposition rate was 0.303 nm/s. The Cu-doped Ag film was deposited by co-sputtering Cu and Ag. The concentrations

of Cu and Ag were controlled by adjusting the sputtering powers of the Cu and Ag targets. The calibrated deposition rates of Ag and Cu were 1.109 and 0.019 nm/s, respectively. The Al_2O_3 film was deposited using an Al_2O_3 target via RF sputtering at a calibrated rate of 0.053 nm/s. The obtained nanocomposite structure was then cut by a laser cutter (with a cutting resolution of ~ 25 μm) to produce the antenna geometries.

Material characterization: The refractive indices and film thicknesses of the deposited layers were characterised by spectroscopic ellipsometry using the interference enhancement method[30,54]. The associated measurement details are presented in Section VIII of the Supporting Information. The optical transmittance was measured using a spectroscopic ellipsometer operating in the transmission mode. The sheet resistance was measured using a four-point probe. The surface morphology of the Cu-doped Ag film was characterised by scanning electron microscopy and atomic force microscopy.

Antenna characterization: Simulations of the antenna properties were conducted using the ANSYS High Frequency Simulation Software (HFSS). Reflection coefficient measurements were performed using a vector network analyser (VNA) that was pre-calibrated in the frequency range of 1−10 GHz. The radiation properties of the antennas were measured inside an anechoic chamber room with the undertest antenna mounted on a controlling machine that could rotate over a range of 360° to capture the entire radiation pattern of the antennas. The transmitted signal was generated using a signal generator with a fixed input power of 20 dBm. A broadband horn antenna with a realised gain of 13 dBi at 2.6 GHz was used as the transmitter antenna. Our undertest antenna was placed 2.5 m away from the transmitter, and the received power was recorded using a spectrum analyser. Finally, the radiation pattern was calculated using the Friis equation.

Acknowledgements
C.Z. would like to thank Ms. Moxin Li for her assistance in editing the figures.

Author details
[1]School of Optical and Electronic Information & Wuhan National Laboratory for Optoelectronics, Huazhong University of Science and Technology, Wuhan, 430074, China. [2]Department of Electrical and Computer Engineering, University of Illinois at Chicago, Chicago, IL 60607, USA. [3]Department of Electrical Engineering and Computer Science, University of Michigan, Ann Arbor, MI 48109, USA

Conflict of interest
The authors declare no conflict of interest.

Supplementary information is available for this paper at https://doi.org/10.37188/lam.2024.036.

Received: 29 June 2023 Revised: 16 June 2024 Accepted: 17 June 2024
Accepted article preview online: 20 June 2024
Published online: 30 June 2024

References

1. Ning, Z. L., Huang, J. & Wang, X. J. Vehicular fog computing: enabling real-time traffic management for smart cities. *IEEE Wireless Communications* **26**, 87-93 (2019).
2. Green, R. B. et al. Optically transparent antennas and filters: a smart city concept to alleviate infrastructure and network capacity challenges. *IEEE Antennas and Propagation Magazine* **61**, 37-47 (2019).
3. Clasen, G. & Langley, R. J. Meshed patch antenna integrated into car windscreen. *Electronics Letters* **36**, 781-782 (2000).
4. Turpin, T. W. & Baktur, R. Meshed patch antennas integrated on solar cells. *IEEE Antennas and Wireless Propagation Letters* **8**, 693-696 (2009).
5. Ha, T. D. et al. Optically transparent metasurface radome for RCS reduction and gain enhancement of multifunctional antennas. *IEEE Transactions on Antennas and Propagation* **71**, 67-77 (2023).
6. Park, J. et al. Soft, smart contact lenses with integrations of wireless circuits, glucose sensors, and displays. *Science Advances* **4**, eaap9841 (2018).
7. Chen, Z. X. et al. Fabrication of highly transparent and conductive indium–tin oxide thin films with a high figure of merit via solution processing. *Langmuir* **29**, 13836-13842 (2013).
8. Liu, H. Y. et al. Transparent conducting oxides for electrode applications in light emitting and absorbing devices. *Superlattices and Microstructures* **48**, 458-484 (2010).
9. Tuna, O. et al. High quality ITO thin films grown by dc and RF sputtering without oxygen. *Journal of Physics D: Applied Physics* **43**, 055402 (2010).
10. Inganäs, O. Avoiding indium. *Nature Photonics* **5**, 201-202 (2011).
11. Na, S. I. et al. Efficient and flexible ITO-free organic solar cells using highly conductive polymer anodes. *Advanced Materials* **20**, 4061-4067 (2008).
12. Pang, S. P. et al. Graphene as transparent electrode material for organic electronics. *Advanced Materials* **23**, 2779-2795 (2011).
13. Bae, S. et al. Roll-to-roll production of 30-inch graphene films for transparent electrodes. *Nature Nanotechnology* **5**, 574-578 (2010).
14. Lee, J. Y. et al. Solution-processed metal nanowire mesh transparent electrodes. *Nano Letters* **8**, 689-692 (2008).
15. Lee, S. Y. et al. Optically transparent nano-patterned antennas: a review and future directions. *Applied Sciences* **8**, 901 (2018).
16. Kosuga, S. et al. Graphene-based optically transparent dipole antenna. *Applied Physics Letters* **110**, 233102 (2017).
17. Kosuga, S. et al. Radiation properties of graphene-based optically transparent dipole antenna. *Microwave and Optical Technology Letters* **60**, 2992-2998 (2018).
18. Yasin, T. & Baktur, R. Bandwidth enhancement of meshed patch antennas through proximity coupling. *IEEE Antennas and Wireless Propagation Letters* **16**, 2501-2504 (2017).
19. Ding, C., Liu, L. Z. & Luk, K. M. An optically transparent dual-polarized stacked patch antenna with metal-mesh films. *IEEE Antennas and Wireless Propagation Letters* **18**, 1981-1985 (2019).
20. Tung, P. D. & Jung, C. W. Optically transparent wideband dipole and patch external antennas using metal mesh for UHD TV applications. *IEEE Transactions on Antennas and Propagation* **68**, 1907-1917 (2020).
21. Zhao, G. Q. et al. Stable ultrathin partially oxidized copper film electrode for highly efficient flexible solar cells. *Nature Communications* **6**, 8830 (2015).
22. Ghosh, D. S. et al. Widely transparent electrodes based on ultrathin metals. *Optics Letters* **34**, 325-327 (2009).

23. Zhang, C. et al. Thin-metal-film-based transparent conductors: material preparation, optical design, and device applications. *Advanced Optical Materials* **9**, 2001298 (2021).
24. O' Connor, B. et al. Transparent and conductive electrodes based on unpatterned, thin metal films. *Applied Physics Letters* **93**, 223304 (2008).
25. Zhang, C. et al. An ultrathin, smooth, and low-loss Al-doped Ag film and its application as a transparent electrode in organic photovoltaics. *Advanced Materials* **26**, 5696-5701 (2014).
26. Gu, D. E. et al. Ultrasmooth and thermally stable silver-based thin films with subnanometer roughness by aluminum doping. *ACS Nano* **8**, 10343-10351 (2014).
27. Zhao, D. W. et al. High-performance Ta_2O_5/Al-doped Ag electrode for resonant light harvesting in efficient organic solar cells. *Advanced Energy Materials* **5**, 1500768 (2015).
28. Zhang, C. et al. High-performance large-scale flexible optoelectronics using ultrathin silver films with tunable properties. *ACS Applied Materials & Interfaces* **11**, 27216-27225 (2019).
29. Zhang, C. et al. High-performance doped silver films: overcoming fundamental material limits for nanophotonic applications. *Advanced Materials* **29**, 1605177 (2017).
30. Zhang, C. et al. Robust extraction of hyperbolic metamaterial permittivity using total internal reflection ellipsometry. *ACS Photonics* **5**, 2234-2242 (2018).
31. Wang, H. Y. et al. Highly transparent and broadband electromagnetic interference shielding based on ultrathin doped Ag and conducting oxides hybrid film structures. *ACS Applied Materials & Interfaces* **11**, 11782-11791 (2019).
32. Wang, H. Y. et al. Transparent perfect microwave absorber employing asymmetric resonance cavity. *Advanced Science* **6**, 1901320 (2019).
33. Zhang, C. et al. Tantalum pentoxide: a new material platform for high-performance dielectric metasurface optics in the ultraviolet and visible region. *Light: Science & Applications* **13**, 23 (2024).
34. Kirsch, N. J. et al. Optically transparent conductive polymer RFID meandering dipole antenna. Proceedings of 2009 IEEE International Conference on RFID. Orlando, FL, USA: IEEE, 2009, 278-282.
35. Hong, S., Kim, Y. & Jung, C. W. Transparent microstrip patch antennas with multilayer and metal-mesh films. *IEEE Antennas and Wireless Propagation Letters* **16**, 772-775 (2017).
36. Grande, M. et al. Optically transparent wideband CVD graphene-based microwave antennas. *Applied Physics Letters* **112**, 251103 (2018).
37. Kosuga, S. et al. Optically transparent antenna based on carrier-doped three-layer stacked graphene. *AIP Advances* **11**, 035136 (2021).
38. Potti, D. et al. A novel optically transparent UWB antenna for automotive MIMO communications. *IEEE Transactions on Antennas and Propagation* **69**, 3821-3828 (2021).
39. Goliya, Y. et al. Next generation antennas based on screen-printed and transparent silver nanowire films. *Advanced Optical Materials* **7**, 1900995 (2019).
40. Hautcoeur, J. et al. Comparison of the microwave performance of transparent wire monopole antennas based on silver films. *Journal of Electronic Materials* **42**, 552-557 (2013).
41. Suh, Y. H. & Chang, K. Low cost microstrip-fed dual frequency printed dipole antenna for wireless communications. *Electronics Letters* **36**, 1177-1179 (2000).
42. Zhang, Z. J. et al. Dual-band WLAN dipole antenna using an internal matching circuit. *IEEE Transactions on Antennas and Propagation* **53**, 1813-1818 (2005).
43. Mohring, B. N., Gabler, B. & Limbach, M. Antenna in-situ performance analysis for the hypersonic flight vehicle HEXAFLY: employing measurement data in a simulation model. *IEEE Antennas and Propagation Magazine* **63**, 89-99 (2021).
44. Huang, J. & Densmore, A. C. Microstrip Yagi array antenna for mobile satellite vehicle application. *IEEE Transactions on Antennas and Propagation* **39**, 1024-1030 (1991).
45. Qian, Y. et al. Microstrip-fed quasi-Yagi antenna with broadband characteristics. *Electronics Letters* **34**, 2194-2196 (1998).
46. Kaneda, N. et al. A broadband planar quasi-Yagi antenna. *IEEE Transactions on Antennas and Propagation* **50**, 1158-1160 (2002).
47. Elsheakh, D. M. & Abdallah, E. A. Ultra wide band planar printed quasi-Yagi antenna with size reduction for water detection in the Egyptian desert. *Microwave and Optical Technology Letters* **57**, 226-233 (2015).
48. Yang, F. et al. Wide-band E-shaped patch antennas for wireless communications. *IEEE Transactions on Antennas and Propagation* **49**, 1094-1100 (2001).
49. Guha, D., Biswas, M. & Antar, Y. M. M. Microstrip patch antenna with defected ground structure for cross polarization suppression. *IEEE Antennas and Wireless Propagation Letters* **4**, 455-458 (2005).
50. Foroozesh, A. & Shafai, L. Investigation into the effects of the patch-type FSS superstrate on the high-gain cavity resonance antenna design. *IEEE Transactions on Antennas and Propagation* **58**, 258-270 (2010).
51. Ge, Y. H., Esselle, K. P. & Bird, T. S. The use of simple thin partially reflective surfaces with positive reflection phase gradients to design wideband, low-profile EBG resonator antennas. *IEEE Transactions on Antennas and Propagation* **60**, 743-750 (2012).
52. Bai, X. D. et al. Radiation-type programmable metasurface for direct manipulation of electromagnetic emission. *Laser & Photonics Reviews* **16**, 2200140 (2022).
53. Bai, X. D. et al. Time-modulated transmissive programmable metasurface for low sidelobe beam scanning. *Research* **2022**, 9825903 (2022).
54. Hilfiker, J. N. et al. Survey of methods to characterize thin absorbing films with spectroscopic ellipsometry. *Thin Solid Films* **516**, 7979-7989 (2008).